

pubs.acs.org/JACS Article

Bulk and Surface Chemistry of the Niobium MAX and MXene Phases from Multinuclear Solid-State NMR Spectroscopy

Kent J. Griffith, Michael A. Hope, Philip J. Reeves, Mark Anayee, Yury Gogotsi, and Clare P. Grey*



Cite This: J. Am. Chem. Soc. 2020, 142, 18924–18935



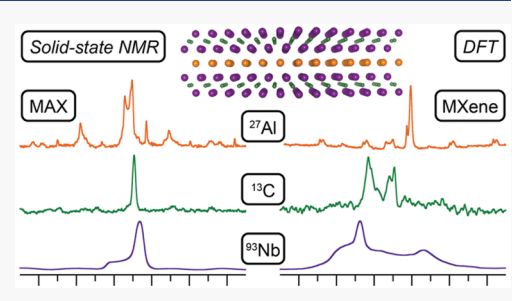
ACCESS

Metrics & More

Article Recommendations

Supporting Information

ABSTRACT: MXenes, derived from layered MAX phases, are a class of two-dimensional materials with emerging applications in energy storage, electronics, catalysis, and other fields due to their high surface areas, metallic conductivity, biocompatibility, and attractive optoelectronic properties. MXene properties are heavily influenced by their surface chemistry, but a detailed understanding of the surface functionalization is still lacking. Solid-state nuclear magnetic resonance (NMR) spectroscopy is sensitive to the interfacial chemistry, the phase purity including the presence of amorphous/nanocrystalline phases, and the electronic properties of the MXene and MAX phases. In this work, we systematically study the chemistry of Nb MAX and MXene phases, Nb₂AlC, Nb₄AlC₃, Nb₂CT_x, and



Nb₄C₃T_x, with their unique electronic and mechanical properties, using solid-state NMR spectroscopy to examine a variety of nuclei (¹H, ¹³C, ¹⁹F, ²⁷Al, and ⁹³Nb) with a range of one- and two-dimensional correlation, wide-line, high-sensitivity, high-resolution, and/ or relaxation-filtered experiments. Hydroxide and fluoride terminations are identified, found to be intimately mixed, and their chemical shifts are compared with other MXenes. This multinuclear NMR study demonstrates that diffraction alone is insufficient to characterize the phase composition of MAX and MXene samples as numerous amorphous or nanocrystalline phases are identified including NbC, AlO₆ species, aluminum nitride or oxycarbide, AlF₃·nH₂O, Nb metal, and unreacted MAX phase. To the best of our knowledge, this is the first study to examine the transition-metal resonances directly in MXene samples, and the first ⁹³Nb NMR of any MAX phase. The insights from this work are employed to enable the previously elusive assignment of the complex overlapping ^{47/49}Ti NMR spectrum of Ti₃AlC₂. The results and methodology presented here provide fundamental insights on MAX and MXene phases and can be used to obtain a more complete picture of MAX and MXene chemistry, to prepare realistic structure models for computational screening, and to guide the analysis of property measurements.

INTRODUCTION

MAX phases (M = early transition metal; A = Al, Si, Ga; X =C, N) are a large class of 3D layered ternary compounds with the stoichiometry $M_{n+1}AX_n$ $(1 \le n \le 4)$. ¹⁻⁴ MXenes are a similarly diverse class of 2D compounds derived from MAX phases via etching of the A-site atoms.⁵ It is well-established that MXenes are surface-terminated, and thus better represented by the formula $M_{n+1}X_nT_x$ (T = termination), however the nature of the surface composition, coordination, and spatial arrangements are exceptionally challenging to ascertain (Figure 1). Both material families have extremely diverse applications: MAX phases are used for industrial components with high temperature applications such as heating elements and gas burner nozzles 1,3,6 and MXenes are being tested as functional materials for applications in energy storage, 7,8 hydrogen 9,10 and oxygen 11,12 evolution catalysis, cancer therapeutics, 13 and electromagnetic interference shielding. 14,15 The electronic and functional properties of MXenes depend strongly on the surface terminations, 16-18 so a deeper understanding of the surface chemistry is required to optimize the performance in these applications.

As the first reported MXene, Ti₃C₂T_x has been the most thoroughly studied member of this family, while many other MXenes have been, and continue to be, synthesized and applied to diverse functions. In this work, on the other hand, we focus on the less studied 4d transition metal-based niobium MAX and MXene phases including Nb₄AlC₃, Nb₄C₃T_x, Nb₂AlC, and Nb₂CT_x, and Nb₂SnC. While Nb₂AlC¹⁹ and Nb₂SnC²⁰ were reported in the 1960s, it was not until the 2000s that Nb₄AlC₃ emerged²¹ via a synthesis strategy borrowed from the synthesis of the Ta MAX series. The syntheses of Nb₂CT_x²² and Nb₄C₃T_x²³ MXenes were then reported in 2013 and 2014, respectively, by selective etching of Al from Nb₂AlC and Nb₄AlC₃, following the same methodology as for Ti₃C₂T_x. Neither the intermediate compound Nb₃AlC₂ nor its MXene derivative have been reported; density

Received: August 22, 2020 Published: October 23, 2020





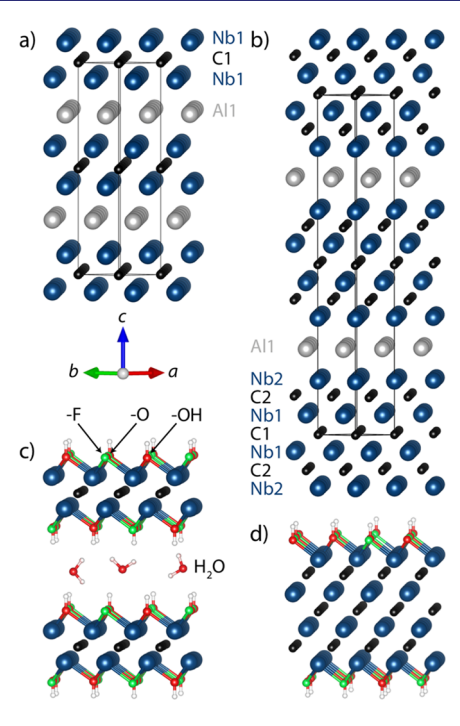


Figure 1. Crystal structures of the niobium MAX and surface-terminated MXene compounds. In (a) Nb₂AlC and (b) Nb₄AlC₃, the crystallographic sites are labeled and the unit cells are outlined. Table 1 describes the local coordination around each atom. The corresponding MXenes (c) Nb₂CT_x and (d) Nb₄C₃T_x, showing -F, -O, and -OH terminations; two layers and interlayer water are shown for Nb₂CT_x.

functional theory (DFT) calculations suggest that this 312 MAX phase is dynamically unstable. The Nb MAX and MXene phases have various interesting properties and potential applications including in biomedical and optical applications. Nb₂CT_x²² and Nb₄C₃T_x²⁷ have attracted recent interest as lithium-ion battery anodes. Nb₄C₃T_x is one of the most conductive and strongest MXene phases, which makes it promising for field-effect transistors and mechanical applications. Nb₂SnC²⁹ and Nb₂AlC³⁰ are superconducting up to 7.8 and 0.440 K, respectively. Superconductivity was recently observed in Nb₂CT_x at 4.5 to 7.1 K, the temperature depending on the surface termination.

The structures of the Nb MAX and MXene phases are shown in Figure 1, with the first-shell coordination numbers and geometry given in Table 1. Nb₄AlC₃ and Nb₄C₃T_x contain two distinct crystallographic Nb sites and two C sites. Nb2 and C2 are the sites nearer to the Al/etched layer and will thus be referred to as "external" while Nb1 and C1 are denoted "internal" following the assignments in the Inorganic Crystal Structure Database crystal structure files 160755^{21} and $606236.^{19}$ Nb₂AlC and Nb₂CT_x contain one Nb site and one

C site; these are necessarily "external". Both MAX phases contain a single Al environment with trigonal prismatic coordination to six niobium atoms. Note that the MXene coordination in Table 1 is described in the absence of termination groups (T).

Solid-state NMR spectroscopy is a versatile toolkit that is sensitive to bonding and electronic properties with the ability to probe different elements individually. Additionally, there is no requirement for long-range periodic order in NMR, therefore, it can be readily applied to defect and surface chemistry as well as to nanoparticles. In particular, NMR can reveal the presence of amorphous impurities which are invisible to diffraction techniques. All of the elements in the niobium aluminum carbide phases are NMR active and relatively accessible: ${}^{13}\text{C}$ is I=1/2 with a natural abundance of 1.1%, while 93 Nb (I = 9/2) and 27 Al (I = 5/2) are 100% naturally abundant quadrupolar nuclei. The quadrupolar nature of the latter two nuclei means that their NMR responses are extremely sensitive to the symmetry of their local environment. Despite the analytical utility, NMR investigations of MAX and MXene phases are sparse. Lue et al. measured static ²⁷Al NMR spectra of the 3d transition metal MAX series Ti₂AlC, V₂AlC, and Cr₂AlC, ³¹ finding relatively long nuclear relaxation times and systematically decreasing nuclear quadrupole coupling constants and Knight shifts from Ti toward Cr. 31 The first NMR study of a MXene was by Harris et al., who identified -OH and -F surface terminations in V₂C by ¹H and ¹⁹F NMR spectroscopy and demonstrated the proximity of ¹H nuclei to the MXene surfaces by using ¹H→¹³C cross-polarization (CP).³² Hope et al. later quantified the concentrations of -OH and -F terminations on Ti₃C₂ MXene, which were found to be highly dependent on the synthesis method, and showed the terminations to be intimately mixed using 1H-19F NMR correlation experiments.³³ ¹H and ¹³C experiments have been extended to further Ti₃C₂T_x syntheses and preparation conditions in a pair of very recent reports. 34,35

In this work, a comprehensive multinuclear NMR study (93Nb, 27Al, 13C, 1H, and 19F) of the bulk structures and surface chemistry of the known Nb_{n+1}AlC_n MAX and Nb_{n+1}C_nT_x MXene phases is performed with a range of one-and two-dimensional techniques, with additional comparisons to Nb₂SnC and the 47/49Ti NMR of Ti₃AlC₂ MAX phase. These experiments are supported by DFT-based electronic structure calculations of the electric field gradient (EFG) at the nucleus. The quadrupolar parameters determined by high-resolution magic-angle spinning (MAS) and static wide-line 93Nb and 27Al spectra give insights on the local structures of the MAX phases, while 93Nb and 13C spectra reveal the nature of the etching to the corresponding MXene phases, with the 93Nb NMR further confirming that the latter are surface terminated. 1H, 19F, and 93Nb two-dimensional NMR spec-

Table 1. Local Atomic Sites in Nb MAX and MXene Phases^a

coordination by crystallographic site						
compound	Nb1	Nb2	Al	C1	C2	
Nb ₂ AlC	fac-NbAl ₃ C ₃ (D)		$AlNb_6(P)$	CNb ₆ (R)		
Nb ₄ AlC ₃	$NbC_6(R)$	fac -NbAl $_3$ C $_3$ (D)	$AlNb_6(P)$	$CNb_6(R)$	$CNb_6(R)$	
Nb_2C	$NbC_3(T)$			$CNb_6(R)$		
Nb_4C_3	$NbC_3(T)$	$NbC_3(T)$		$CNb_6(R)$	$CNb_6(R)$	

 $^{^{}a}D$ = distorted octahedron; R = regular octahedron; T = trigonal pyramid; P = prismatic.

troscopy then identifies the chemistry and connectivity of the MXene surface terminations. Finally, the presence of diffraction-silent side-products is confirmed, including the observation of aluminum oxides via the ²⁷Al NMR spectra. Overall, these results have important implications for the synthesis, characterization, and functional properties of Nb MAX and MXene phases.

■ EXPERIMENTAL SECTION

Synthesis. Nb₂AlC MAX phase was prepared as described per Naguib et al. ²² Elemental powders of niobium (99.9% metals basis, 325 mesh), aluminum (99.8% purity, 300 mesh), and carbon black (99% purity, 300 mesh) were mixed in a plastic jar with a ratio of 2:1.1:1 Nb:Al:C and ball milled. The powder was placed into an alumina boat and heated under Ar flow to 1600 °C, with a ramp rate of 4 °C min⁻¹, and sintered for 4 h. After natural cooling to room temperature, the MAX phase was milled into powder and sieved through a 400-mesh sieve.

To prepare Nb₂CT_x MXene, 1.0 g of Nb₂AlC powder was transferred into 20 mL of HF (aqueous, 49%, Millipore-Sigma) over 60 s and stirred for 48 h at 50 °C. The mixture was washed several times by centrifugation at 3500 rpm (5 min/cycle), the supernatant was decanted, and deionized (DI) water was added until the supernatant reached a pH > 6. Multilayered MXene powder was collected by filtration through a cellulose acetate membrane (0.45 μ m pore size). The delamination of Nb₂CT_x was carried out by transferring 1.0 g of MXene powder into 10 mL of a diluted tetramethylammonium hydroxide (TMAOH) solution (25% in H₂O, Millipore-Sigma). The solution was stirred overnight (\sim 18 h) at room temperature. To remove excess TMAOH, the mixture was washed by centrifugation with DI water (50 mL) at 3500 rpm for 20 min followed by decantation of the supernatant. The process was repeated until the supernatant reached a pH < 8. Then, the sediment was dispersed in 50 mL of deionized water and sonicated for 1 h in an icebath with Ar bubbling. Finally, the mixture was centrifuged for 1 h at 3500 rpm, and the supernatant was carefully removed to leave the MXene sediment in the bottom of the tube.

To prepare Nb₄AlC₃, powders of niobium (99.9% metals basis, 325 mesh), aluminum (99.8% purity, 300 mesh), and carbon black (99% purity, 300 mesh) were mixed, and the synthesis was performed as previously reported. To prepare Nb₄C₃T_x, 0.4 g of Nb₄AlC₃ powder was added to 30 mL of HF solution (aqueous, 49%, Millipore-Sigma) and stirred at room temperature (20–25 °C) for 6 days. The produced acidic mixture was washed by DI water followed by centrifugation (3500 rpm, 2 min per cycle). After each centrifugation cycle, the supernatant was discarded, and the sediment was dispersed in DI water until neutral pH (\sim 7) was reached. In order to delaminate the Nb₄C₃T_x, 1 mL of TMAOH (25% in H₂O, Millipore-Sigma) was mixed with 9 mL of DI H₂O, added to Nb₄C₃T_x, and shaken for 15 min at room temperature. The excess TMAOH was separated from the product by repeated centrifugation at 3500 rpm.

Diffraction. X-ray diffraction (XRD) patterns were recorded in reflection mode under sample rotation on a PANalytical Empyrean diffractometer with a Cu K α (1.540598 Å + 1.544426 Å) X-ray source.

Solid-State NMR Spectroscopy. ¹H, ¹³C, and ¹⁹F spectra were recorded at 11.75 T. ¹H and ¹⁹F spectra were recorded with a Hahn echo pulse sequence or by taking the isotropic slice of a magic angle turning, phase adjusted spinning sideband (MATPASS) sideband-separation experiment. ³⁶ ¹H and ¹⁹F experiments were performed at 50 kHz MAS in a 1.3 mm HX probe with recycle delays of 15 and 0.3 s, respectively. ¹³C spectra were recorded in a 2.5 mm HX probe at 25 kHz MAS, with a 1 s recycle delay and a Hahn echo pulse sequence; the MAX samples were diluted with 20 wt % boron nitride to facilitate spinning (of these metallic samples). ¹H/⁹³Nb and ¹⁹F/⁹³Nb TRAPDOR experiments were performed at 25 kHz with a 2.5 mm HX probe and a recycle delay of 1 s. ¹H/¹⁹F HECTOR experiments were performed at 20 kHz with a 2.5 mm HX probe with recycle delays of 1 or 3 s. ²⁷Al and ⁹³Nb spectra were recorded at 16.4 T with

a 1.3 mm or 4.0 mm HXY probe under static or MAS conditions with a single pulse or a Hahn echo pulse sequence and a recycle delay of 0.3–100 s for ²⁷Al and 0.1–0.5 s for ⁹³Nb, as described in each figure. Broad static ⁹³Nb spectra were collected with the assistance of an external automatic tuning/matching (eATM) robot.³⁷ These variableoffset cumulative spectra (VOCS) measurements were recorded in steps of 170 kHz (~1000 ppm). 47,49Ti spectra were recorded with a CPMG pulse sequence using VOCS acquisition in steps of 80 kHz (~2000 ppm) with 115 echoes of 0.8 ms each and recycle delays of 0.1 s; the subspectra were combined by taking the skyline projection:³⁸ for each point, the highest intensity value from the overlapping subspectra is taken, rather than adding their intensities together. ¹H spectra were referenced to adamantane at 1.81 ppm, ¹³C spectra to the tertiary carbon of adamantane at 38.5 ppm, ¹⁹F spectra to LiF at -203 ppm, ²⁷Al spectra to AlF₃ at -15 ppm, ⁹³Nb spectra to LiNbO₃ at -1004 ppm, ³⁹ and ^{47/49}Ti spectra to the ⁴⁹Ti signal of SrTiO₃ at -843 ppm.

The isotropic shift $\delta_{\rm iso}$ is defined in the Haeberlen convention $\delta_{\rm iso} = \frac{\delta_{\rm XX} + \delta_{\rm YY} + \delta_{\rm ZZ}}{3}$ with the chemical shift anisotropy $\delta_{\rm CSA}$ defined as $\delta_{\rm CSA} = \delta_{\rm ZZ} - \delta_{\rm iso}$ and the shift asymmetry $\eta_{\rm CSA}$ defined as $\eta_{\rm CSA} = \frac{\delta_{\rm YY} - \delta_{\rm XX}}{\delta_{\rm ZZ} - \delta_{\rm iso}}$. With these definitions, the principal components of the shift tensor are ordered such that $|\delta_{\rm ZZ} - \delta_{\rm iso}| \geq |\delta_{\rm XX} - \delta_{\rm iso}| \geq |\delta_{\rm YY} - \delta_{\rm iso}|$. N.b. This definition of $\delta_{\rm CSA}$ is sometimes referred to as the reduced anisotropy, which is equal to 2/3 of the "full" anisotropy $\Delta\delta = \delta_{\rm ZZ} - \frac{\delta_{\rm XX} + \delta_{\rm YY}}{2}$ used by some authors and programs. The quadrupolar coupling constant, $C_{\rm Q}$, is defined by the nuclear quadrupole moment Q ($Q_{\rm Nb-93} = 32(2)$ fm²; $Q_{\rm Al-27} = 14.66(10)$ fm²) and the largest principal component $V_{\rm ZZ}$ of the EFG at the nucleus according to $C_{\rm Q} = \frac{eQV_{\rm ZZ}}{h}$ where e is the electric charge and h is Planck's constant. The quadrupolar asymmetry parameter $\eta_{\rm Q}$ is also defined by the EFG tensor components as $\eta_{\rm Q} = \frac{V_{\rm XX} - V_{\rm YY}}{V_{\rm ZZ}}$ ordered such that $|V_{\rm ZZ}| \geq |V_{\rm YY}| \geq |V_{\rm XX}|$. The Rose convention (ZYZ) was used to define the Euler angles relating the orientations of the shift and quadrupolar tensors.

Calculations. Density functional theory (DFT) calculations were performed with the CASTEP planewave pseudopotential code. ⁴¹ The calculations used the Perdew–Burke–Ernzerhof (PBE) exchange–correlation functional ⁴² and Vanderbilt ultrasoft pseudopotentials. ⁴³ MAX crystal structures were used as starting models. ^{19,21} Prior to the EFG calculations, atomic positions were optimized (with lattice parameters held constant) until the force on any atom was smaller than 10 meV Å⁻¹. All calculations used a planewave energy cutoff energy of 600 eV and a Monkhorst–Pack ⁴⁴ grid with a spacing finer than $2\pi \times 0.04$ Å⁻¹ to sample the Brillouin zone. Computed EFG parameters were used as the starting point to fit the experimental ²⁷Al and ⁹³Nb spectra.

RESULTS AND DISCUSSION

MAX Bulk Structure Characterization. XRD analysis of the Nb₂AlC sample (Figure S1) showed Nb₄AlC₃ as a minor (\sim 5% from Rietveld refinement) secondary phase. No additional peaks were visible beyond those of the two MAX phases. The Nb₄AlC₃ diffraction pattern showed a NbC-like impurity (\sim 8%) and a small, broad unindexed peak just above the background signal at 26.7°; no Nb₂AlC was detected in the Nb₄AlC₃ sample.

²⁷Al NMR spectra of the MAX phases Nb₂AlC and Nb₄AlC₃ are given in Figures 2 and 3, respectively. For each compound, a simultaneous fit was performed over the static and MAS spectra (Table 2). The DFT calculated quadrupolar parameters served as useful starting points to guide the fits. Static spectra were sensitive to the value of the CSA while MAS removed CSA broadening and resulted in spectra that were more sensitive to the isotropic shift and quadrupolar tensor.

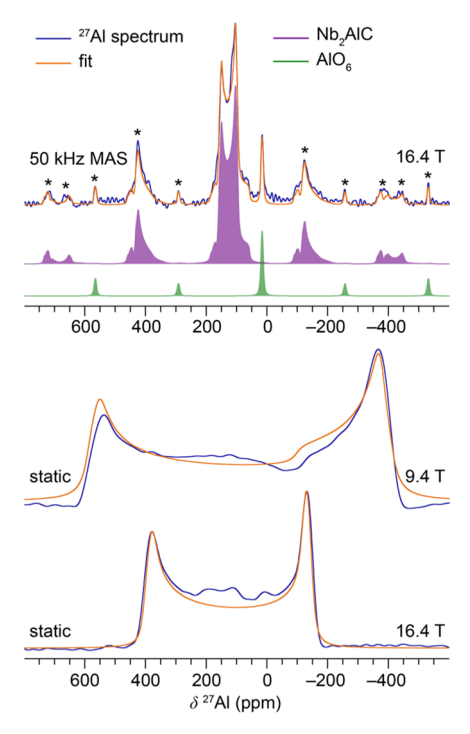


Figure 2. ²⁷Al NMR spectra of Nb₂AlC at 50 kHz MAS (top) and static (bottom). MAS rate and magnetic field are given for each spectrum. The recycle delays were 100 and 0.35 s for the MAS and static spectra, respectively. The static spectra were T_1 -filtered to facilitate efficient recording of the fast-relaxing MAX signal whereas the MAS spectrum was recorded under quantitative conditions to observe all aluminum environments. Spinning sidebands are denoted with asterisks. See Table 2 for fitting parameters.

The positions of discontinuities in the powder line shape from satellite transitions, where observed, were also used to determine the quadrupolar parameters. The calculated quadrupolar coupling constants matched the experimental values to within <5%.

In addition to aluminum in the MAX phases, ²⁷Al NMR revealed the presence of secondary phases. At short recycle delays, the MAX phases, with fast spin-lattice (T_1) nuclear relaxation from conduction electrons, appear relatively pure (Figure S2-3). However, at longer free induction decay (FID) intervals, the relative intensities of the impurities increase; an indication that the impurities are diamagnetic with longer T_1 relaxation times. The Nb₂AlC sample exhibits an unexpected resonance at 16 ppm while the Nb₄AlC₃ sample shows three additional ²⁷Al resonances at ca. 5, 17, and 115 ppm. The largest impurity in both samples is ascribed to octahedral AlO₆ environments as found in corundum alumina, 45 on the basis of the shift (16-17 ppm), $C_{\rm O}$ (ca. 2.4 MHz, upper limit \leq 4 MHz) and T_1 relaxation time (18 s). The Nb₄AlC₃ sample signal at 5 ppm is also consistent with octahedral AlO₆, as found in, e.g., boehmite, gibbsite, or γ -alumina. 46 The oxide environments could arise from secondary oxide phases or from the oxide layers previously observed by XPS to form on the surface of MAX particles.⁴⁷ The resonance at 115 ppm appears at a higher frequency than for typical aluminum oxides or fluorides; 48 it does coincide with the shift range of aluminum carbide Al₄C₃ (111–120 ppm) but the maximum C_0 value for the observed resonance is ca. 4.5 MHz while Al_4C_3 has two Al sites with C_Q magnitudes of 14–17 MHz.^{49,50} Hayes et al. identified aluminum oxycarbide impurities with smaller C_{O} s in

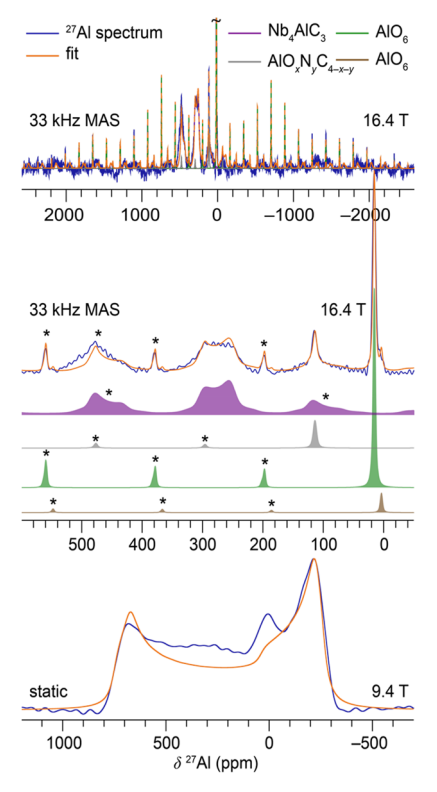


Figure 3. ²⁷Al NMR spectra of $\mathrm{Nb_4AlC_3}$ at 33 kHz MAS (top and middle) and static (bottom). Note the different *x*-axis scales. MAS rate and magnetic field are given for each spectrum. The recycle delays were 90 and 0.05 s for the MAS and static spectra, respectively. Spinning sidebands are denoted with an asterisks. See Table 2 for fitting parameters. The missing intensity in the fit of the static spectrum is ascribed to the $\mathrm{AlO_6}$ environment at ~ 16 ppm.

their recent study of commercial Al₄C₃ so a related aluminum species is plausible here. 50 Another possibility is the tetrahedral aluminum nitride environment that appears at around 110-115 ppm in AlN and in aluminum oxynitrides with a C_Q of a few MHz, consistent with the resonance observed here. Note that the 27 Al signal from Nb₂AlC covers a range of ~ 90 – 170 ppm, so the impurity at 115 ppm is less pronounced but it can be clearly seen as a shoulder that appears as the interval between scans increases (Figure S2). Quantitative spectra recorded with recycle delays of 90-100 s (Figure S2) revealed the relative ratios of the MAX and impurity (or surface) species in the samples from the perspective of aluminum content.⁴⁷ For the Nb₂AlC sample, a ratio of 89:9:2 was found for the MAX signal at 169 ppm and the impurity resonances at 16 and 115 ppm, respectively. For the Nb₄AlC₃ sample, a ratio of 56:34:7:3 was found for the MAX signal at 319 ppm and the impurity resonances at 17, 5, and 115 ppm, respectively.

Quadrupolar ⁹³Nb NMR spectra of the compounds were recorded under MAS and static conditions. A fit of the ⁹³Nb NMR data of Nb₂AlC reproduced the central and satellite transitions of the spectrum (Figure 4 and Table 2), with calculated and measured nuclear quadrupolar coupling constants in close agreement. The Hahn echo and quadrupolar Carr–Purcell–Meiboom–Gill (QCPMG) ⁹³Nb MAS spectra of Nb₄AlC₃ (Figure 5b,c) showed a number of overlapping peaks that could not be resolved by variable MAS rates due to their individual linewidths (full-width at half-maximum > 40 kHz), and the static spectrum also showed overlapping lineshapes (Figure S4). To overcome this challenge, a

Table 2. Experimental (Shift and Quadrupolar) and Calculated (Quadrupolar Only) NMR Parameters of Nb_2AlC and $Nb_4AlC_3^a$

					$C_{\mathbb{Q}}$ (N	⁄IHz)	η_{Q}		
phase	site	δ_{iso} (ppm)	$\delta_{ ext{CSA}}$	η_{CSA}	exp.	calc. ^b	exp.	calc.	Euler angles β (deg) ^c
Nb ₂ AlC	Nb1	$-475(10)^d$	280(50)	0.1(1)	32.3(3)	-30.8	0.01(1)	0.00	5(2)
	Al1	171(2)	-275(20)	0.2(1)	15.7(2)	-16.0	0.05(5)	0.00	2(5)
	C1	293(1)	n/d	n/d					
Nb ₄ AlC ₃	Nb1	-1700(5)	300(200)	0.0(1)	2(1)	2.5	n/d	0.00	n/d
	Nb2	-840(20)	650(200)	0.0(1)	32(5)	-33.5	0.00(5)	0.00	80(10)
	Al1	319(2)	-280(10)	0.4(2)	15.6(2)	-16.0	0.10(10)	0.00	0(5)
	C1	238(2)	n/d	n/d					
	C2	324(2)	n/d	n/d					

"See Table S1 for chemical shift tensor component values in the standard convention. Static and magic angle spinning spectra (in some cases at multiple fields) were fit to a single model. Estimated errors in the last digit are given in parentheses, derived from line shape fitting. n/d = not determined, either due to insufficient signal-to-noise (13 C) or because the fit was insensitive to this parameter. Cells corresponding to the quadrupolar properties are left blank for 13 C because it is a I = 1/2 nucleus. b The sign of the quadrupolar coupling can be calculated but is not determined experimentally from the spectrum of a polycrystalline sample. c The fits are only sensitive to the β angle because η is nearly zero. d The isotropic shift is temperature-dependent and thus varies with MAS rate. The static 93 Nb spectrum of Nb₂AlC was fit with -475(10) ppm while the 50 kHz spectrum was fit with -445(5) ppm.

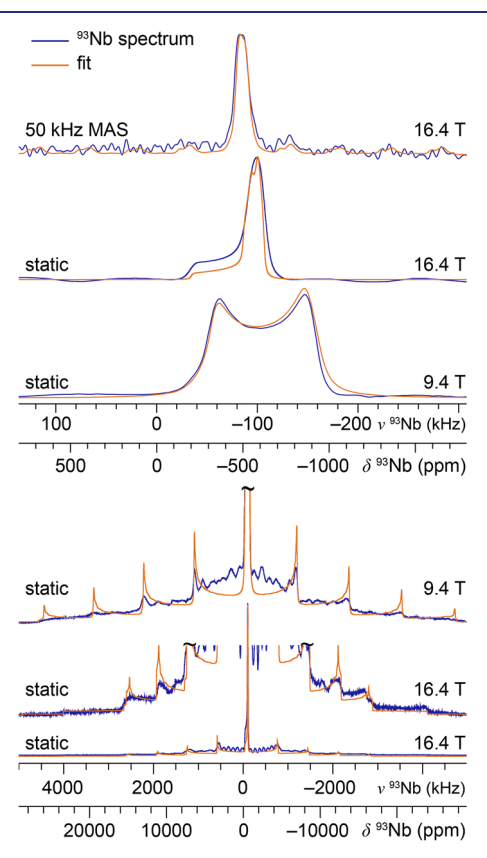


Figure 4. 93 Nb NMR spectra of Nb₂AlC. MAS rate and magnetic field are given for each spectrum. See Table 2 for fitting parameters.

MATPASS experiment was performed; the isotropic slice showed three broad, featureless resonances at -840, -1700, and -2340 ppm (Figure 5a). However, only two distinct Nb environments are expected in Nb₄AlC₃. The low frequency ⁹³Nb resonance matches that of NbC (Figure 5a,b, Figure S5a), as do the ¹³C NMR data (vide infra). Stoichiometric NbC should give a sharp ⁹³Nb signal with $C_Q = 0$ due to the cubic site symmetry of the 12-coordinate niobium atom, however nonstoichiometry is common in NbC, ⁵⁵ depending on the preparation conditions, with NbC_x (0.7 $\leq x < 1$) yielding quadrupolar ⁹³Nb signals. ^{56,57} Overlapping lines

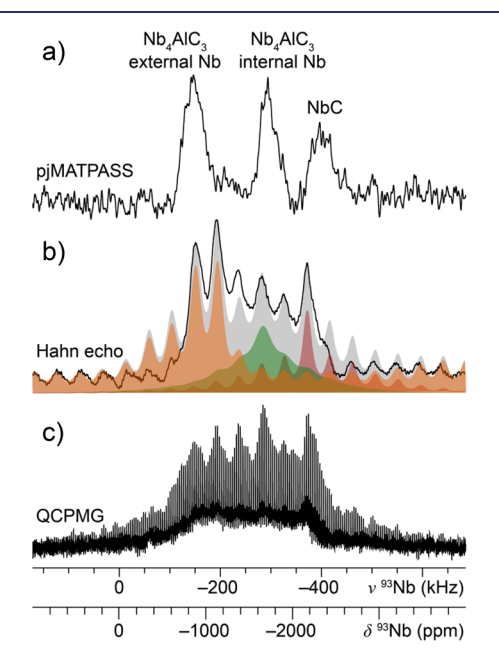


Figure 5. 93 Nb MAS NMR spectra of the Nb₄AlC₃ sample (45 kHz MAS, 16.4 T). Several methods were used to study this sample including (a) the isotropic slice of a pjMATPASS experiment; (b) a Hahn echo, deconvoluted in gray with the internal site Nb1 in green, the external site Nb2 in orange, and NbC in red; and (c) a QCPMG measurement.

preclude an accurate fitting of the quadrupolar parameters of the $\mathrm{NbC_x}$ impurity in $\mathrm{Nb_4AlC_3}$ here but a small C_Q (~2 MHz) is consistent with the line shape. For $\mathrm{Nb_2SnC}$ (Figure S6), a sharp $^{93}\mathrm{Nb}$ signal was observed with an isotropic shift of -189(3) ppm; this is 300 ppm higher frequency than the isostructural $\mathrm{Nb_2AlC}$. In the wide-line static VOCS measurement, Nb metal was also observed as a secondary phase at ~7200 ppm.

The ¹³C NMR spectrum of Nb₂AlC (Figure 6a, bottom) shows a single resonance at 293 ppm corresponding to the single carbon environment in the 211 phase. The ¹³C NMR spectrum of Nb₄AlC₃ (Figure 6b, bottom) shows two resonances at 324 and 238 ppm corresponding to the outer (C2) and inner (C1) carbon sites of Nb₄AlC₃, respectively. For

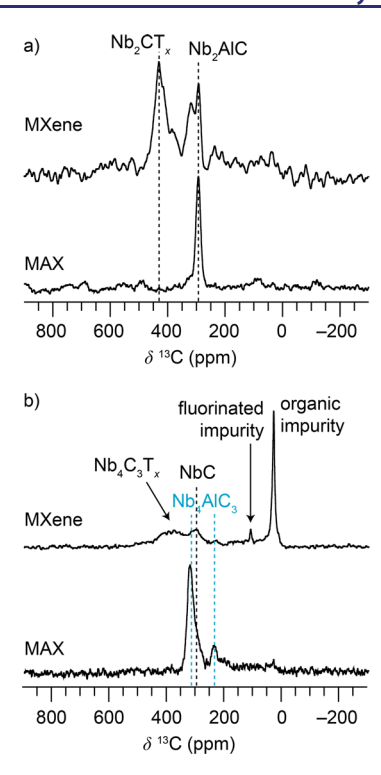


Figure 6. ¹³C NMR spectra of (a) Nb₂CT_x MXene and Nb₂AlC MAX phase and (b) Nb₄C₃T_x MXene and Nb₄AlC₃ MAX phase at 25 kHz MAS and 16.4 T. Resonances are labeled, and dashed lines are guides to the eye.

both Nb MAX phases, the large ¹³C shift is evidence of metallic conduction resulting in a Knight shift; the shifts are larger than observed for V₂AlC (208 ppm)³² but less than for Ti₃AlC₂ (566 ppm).³³ There is a significant shoulder for the 324 ppm peak which is ascribed to NbC, the single carbon site of which resonates at ~315 ppm (Figure S5b,c); accounting for this signal, the integrated intensities of the inner and outer carbon sites are in reasonable agreement with the expected 2:1 ratio. The ¹³C and ⁹³Nb data together clearly show the presence of NbC in Nb₄AlC₃, although it is not easily observed in the Xray diffraction pattern (Figure S1) because (i) it is present in nanoparticulate or amorphous form and/or (ii) its identification is obstructed by peak overlap. Note that phases such as amorphous carbon and low levels of Nb2O5 would be difficult to observe via these NMR experiments due to the broad nature of those signals and/or overlap with other signals. The presence of alumina suggests that niobia could also be present, and Sarycheva and Gogotsi observed amorphous carbon and titania in a degraded Ti₃C₂T_x sample via Raman spectroscopy.⁵⁸

MXene Bulk Structure Characterization. By etching out the aluminum, the MAX phases were converted to MXenes. However, the Nb₂CT_x also has a significant amount of unreacted Nb₂AlC, while NbC remains present as an impurity in Nb₄C₃T_x, as previously seen for other MAX/MXene samples. 23,59

The 93 Nb NMR spectra of Nb₂CT_x and Nb₄C₃T_x are shown in Figure 7 and Figure S7. Since niobium atoms are located at the outer surface of the 2D MXene sheets, the number of distinct Nb local environments and NMR signals depends on the surface terminations. The 93 Nb line shape of Nb₂CT_x was simulated with two quadrupolar lines, providing a reasonable fit to the data (Figure 7); the minor but sharper signal is

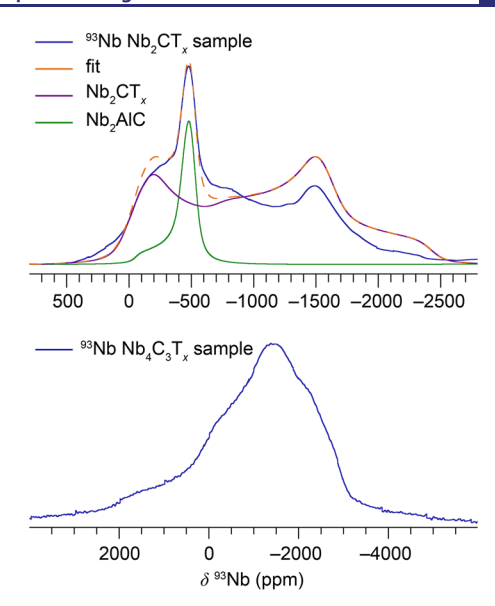


Figure 7. Static ⁹³Nb NMR central transition spectra of the Nb₂CT_x and Nb₄C₃T_x samples at 16.4 T. For Nb₂CT_x, the deconvolution into signals from Nb₂CT_x and Nb₂AlC is shown. For full VOCS spectra, see Figure S7.

consistent with Nb₂AlC, the broader signal was attributed to Nb₂CT_x and was fit with $\delta_{iso} = -790(30)$ ppm, CSA = -350(50) ppm, $\eta_{CSA} = 0.5(3)$, $C_Q = 77(3)$ MHz, $\eta_Q = 0.2(1)$, and Euler angles of α , β , and γ being 0° , $50(10)^{\circ}$, and 0° . The C_0 for Nb₂CT_x is more than double that of Nb₂AlC, providing spectral evidence for the reduction of symmetry at the MXene surface. Furthermore, the nonzero $\eta_{\rm O}$ indicates a breaking of the 3-fold symmetry of the Nb site at the surface, presumably due to the surface terminations. Calculations for a bare Nb₂C surface predict a ^{93}Nb C_{O} of 122 MHz, so the lower observed C_0 is also evidence for the surface terminations which result in a more symmetric charge distribution than a bare surface. Basic ordered models for surface-terminated Nb₂CT_x ($T_x = F_2$) $(OH)_2$, (OH)F, O_2 , and O) give calculated C_Q values ranging from 36-109 MHz (Table S2), which are consistent with the experimental C_O of 77 MHz. The best agreement is for fluoride and oxide termination, which may suggest a greater proportion of fluoride and oxide terminations than hydroxyl terminations, as previously observed for Ti₃C₂T_x. ³³ Meanwhile, the ⁹³Nb line shape of Nb₄C₃T_x is substantially broader. An exact fitting of the line shape could not be obtained due to the difficulty of distinguishing a potential distribution of surface terminations, the two Nb sites in $Nb_4C_3T_x$ and the NbC_x impurity, which all overlap. Nevertheless, based on the line width a maximum C_{O} of ~100 MHz can be determined, ruling out a significant proportion of bare surface (calculated $C_Q = 135$ MHz for the outer Nb2 site, Table S3). Given that the calculated quadrupolar parameters for ordered models of surface terminations (Table S3) are in the range of 15-70 MHz, chemical shift dispersion and anisotropy of the different Nb environments must make a large contribution to the experimental line width.

In the 13 C NMR spectra of etched Nb₂AlC, a new signal can be seen at 430 ppm due to Nb₂CT_x MXene, although there is also still unreacted Nb₂AlC present (Figure 6a, top). The intensity in the 13 C spectrum at frequencies between the Nb₂AlC and Nb₂CT_x resonances may correspond to partially etched regions with carbon environments intermediate

between the MAX and MXene, e.g., regions with a MAX-like aluminum layer on one side but terminations on the other or nanoscale clusters of unetched aluminum. After etching Nb₄AlC₃ (Figure 6b, top), a broad high frequency signal can be observed at ~400 ppm, corresponding to Nb₄C₃T_x MXene, although the inner and outer carbon sites cannot be resolved. After etching, the NbC impurity is still evident, as well as signals from other impurities in the sample at 31 and 111 ppm; the former is correlated with a ¹H signal at 1 ppm in the ¹H→¹³C HETCOR spectrum (Figure S8c), suggesting that this impurity is predominantly alkyl, while the latter can be observed in a ${}^{19}\text{F} \rightarrow {}^{13}\text{C}$ cross-polarization (CP) experiment (Figure S8b), which, combined with the chemical shift, suggests a -CF₂- moiety in a fluorinated organic species. Notably, the ¹³C shift increases on etching from the MAX to the MXene for both Nb₂CT_x and Nb₄C₃T_x; this is due to an increased Knight shift, corresponding to an increased density of states at the Fermi level for the carbon atoms in the MXene phases. The same increase in ¹³C shift was observed for V₂CT_x (from 208 to 260 ppm); 32 however, in contrast, the 13C Knight shift actually decreases for Ti₃C₂T_x (from 566 ppm to 380-410 ppm). 33 A decrease in 13C shift was also observed on etching Mo₂Ga₂C to Mo₂CT_x (from 178 to 125 ppm),⁶¹ although in this case the shift is well within the diamagnetic range, implying there is not a significant density of states at the Fermi level localized on the carbons.

As seen from the presence of the Nb₂AlC MAX signal in the 93 Nb, 27 Al, and 13 C spectra, not all aluminum had been etched out during the HF treatment, consistent with prior work on other MXenes: V₂AlC was observed in V₂CT_x samples and Ti₃AlC₂ in Ti₃C₂T_x samples in their respective 13 C NMR spectra. 32,33 The 27 Al NMR spectra of the MXene samples (Figure S9) also show an AlO₆-like aluminum oxide environment, while the Nb₂CT_x sample also shows a signal consistent with AlF₃·nH₂O, a common impurity in MXenes 60 and one that can be readily identified with NMR spectroscopy.

Since diffraction did not reveal the Al–O, Al–F, or Al–(C,N,O) compounds identified here, these secondary phases must be amorphous, present as small nanoparticles, or hidden under the MAX/MXene diffraction peaks. These findings again highlight that the picture from diffraction alone can be misleading. Furthermore, NbC $_x$ was almost entirely hidden under the Nb $_4$ AlC $_3$ XRD peaks. A method that is sensitive to amorphous phases such as solid-state NMR and/or quantitative diffraction with an internal standard should be routinely performed to characterize MAX and MXene phases.

Surface Terminations of Nb₄C₃T_x and Nb₂CT_x. ¹H and ¹⁹F NMR spectra were recorded in order to investigate the surface functionalization of the MXene phases directly. The ¹H NMR spectrum of Nb₂CT_x as synthesized shows a large signal at 6.3 ppm due to free H₂O as well as two resonances at large chemical shifts of 19.5 and 26.0 ppm (Figure 8a); these latter signals are assigned to -OH surface terminations. -OH terminations were observed in the MXenes V₂CT_x at 85 and 27 ppm³² and $Ti_3C_2T_r$ between 12.5 and 20 ppm, the exact shift values depending on the synthesis procedure. 33,34 The free H₂O signal can be reduced by drying the MXene at 200 °C in vacuo (Figure 8b), after which an additional resonance can be distinguished at 12.2 ppm, as well as sharper signals between -0.5 and +1.6 ppm; the former could be due to a further -OH termination environment, or bound H2O partaking in strong hydrogen bonding, while the latter are

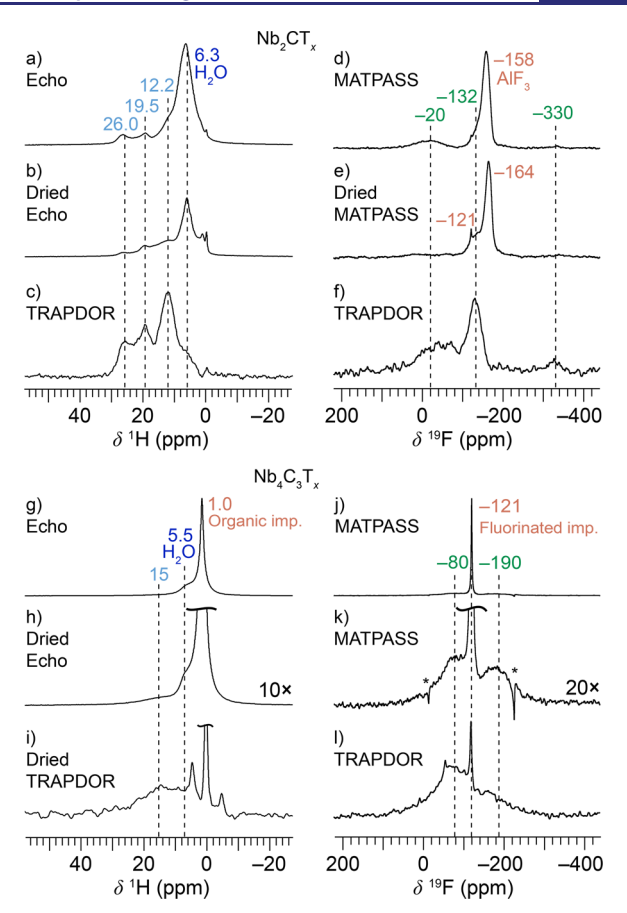


Figure 8. 1 H and 19 F NMR spectra of Nb₂CT_x (a–f) and Nb₄C₃T_x (g–l). The 1 H/ 93 Nb and 19 F/ 93 Nb TRAPDOR difference spectra (c, f, i, and l) show 1 H (c and i) or 19 F (f and l) atoms near 93 Nb atoms. The echo and MATPASS experiments were performed at 50 kHz MAS and the TRAPDOR experiments at 30 kHz, all at a magnetic field strength of 11.7 T. Sidebands are marked with asterisks.

assigned to intercalated volatile contaminants, as was also observed for Ti₃C₂T_x. There is also a loss of intensity for the 26.0 ppm signal in particular, which may be due to loss of –OH terminations as H₂O during the drying process.⁶²

The assignment of the ¹H NMR resonances at high chemical shift to surface species on the MXene layers can be confirmed by ¹H/⁹³Nb TRAPDOR experiments: ⁶³ for these spectra, a ¹H spin echo is recorded with continuous irradiation of 93Nb during only the first half of the echo; thus, any dephasing due to recoupled ¹H-⁹³Nb interactions is only partially refocused, resulting in a loss of signal intensity for ¹H environments in the vicinity of ⁹³Nb; when the difference is taken between spin echoes recorded with and without 93Nb irradiation, these 1H environments (near 93Nb) can be selectively observed. The signals at 12.2, 19.5, and 26.0 ppm can all be clearly observed in the TRAPDOR difference spectra (Figures 8c and S10), confirming their vicinity to Nb atoms at the MXene surface. The signals at less than 5 ppm, on the other hand, are suppressed in the TRAPDOR difference spectra. A weaker TRAPDOR effect is observed for the free H₂O resonance at 6.3 ppm, which suggests that only some of the free H₂O is proximal to Nb and/or that it is mobile; this may be evidence of chemisorbed water, as proposed by Persson et al.⁶⁴

The sideband-separated ¹⁹F NMR spectrum of Nb₂CT_x, recorded with a MATPASS pulse sequence, ⁴⁰ shows a number of different resonances (Figure 8d). The signal at -158 ppm is

due to $AlF_3 \cdot nH_2O$, a byproduct of the etching process also seen in the ^{27}Al spectrum (Figure S9); 33,65 this resonance is suppressed in the ¹⁹F/⁹³Nb TRAPDOR difference spectrum (Figure 8f), leaving the signals at -20, -132, and -330 ppm, which must be near Nb. ¹H/¹⁹F HETCOR experiments (Figure S11) are completely dominated by the $H_2O \leftrightarrow AlF_3$ correlation, so cannot be used to aid assignment of the ¹⁹F spectrum. After drying at 200 °C in vacuo the AlF₃·nH₂O resonance shifts to -164 ppm due to changes in hydration, so that the -132 ppm signal can be seen as a shoulder more clearly, and there is also a small, sharp peak at -121 ppm from a fluorinated organic impurity. The ^{19}F signal at -20 ppm is largely removed by drying, so may be tentatively ascribed to -F terminations with strong hydrogen bonding to H₂O molecules or adjacent -OH terminations (given that the intensity of the -OH signals in the ¹H NMR also decreases on drying). Conversely, the major ¹⁹F signal at -132 ppm is assigned to -F terminations without strong H-bonding. The minor signal at -330 ppm is strongly ionic; it may be a niobium fluoride species formed as a byproduct from excessive etching and could therefore be minimized by using milder etching conditions.66

The 1 H NMR spectrum of Nb₄C₃T_x (Figure 8g) is dominated by a peak at 1.0 ppm due to the organic impurity identified from the 1 H \rightarrow ¹³C HETCOR experiment (Figure S8c). Further 1 H signals at 5.5 and 15 ppm are assigned to H₂O and $^-$ OH terminations, respectively. Both the organic contaminant and the H₂O signals can be reduced by drying in vacuo at 200 $^{\circ}$ C overnight (Figure 8h), while the $^-$ OH terminations can be identified in the 1 H/ 93 Nb TRAPDOR difference spectrum (Figures 8i and S10). In the TRAPDOR experiment, the 1.0 ppm peak is almost, but not entirely, suppressed; the residual signal and satellite peaks are due to the differential phase (Bloch—Siegert) shift 67,68 introduced by 93 Nb irradiation, which results in imperfect cancellation in the difference spectrum.

The ¹⁹F MATPASS NMR spectrum for Nb₄C₃T_x is dominated by a resonance at -121 ppm (Figure 8j,k), which is consistent with the fluorinated impurity identified by $^{19}\text{F} \rightarrow ^{13}\text{C}$ CP. Two other signals can also be distinguished, centered at ca. -190 and -80 ppm; these are assigned to -F terminations as they can clearly be observed in the ¹⁹F/⁹³Nb TRAPDOR difference spectrum (Figure 81), although the sidebands of the terminal -F signals are unresolved. Further evidence for the assignment of the -OH and -F terminations can be seen in the ${}^{1}H/{}^{19}F$ HETCOR spectra: in the ${}^{19}F \rightarrow {}^{1}H$ spectrum (Figure 9b) a broad correlation is observed between both the H₂O (6.0 ppm) and -OH (15 ppm) ¹H resonances and ¹⁹F intensity between ca. +50 and -300 ppm that corresponds to the signals from -F terminations at -190 and -80 ppm, with unresolved spinning sidebands. This supports the assignments of the ¹H and ¹⁹F spectra, as well as showing that the terminations are intimately mixed, rather than being segregated into different regions, as also found for Ti₃C₂T_x. In contrast, the ¹H→¹⁹F spectrum (Figure 9a) only shows correlation between the ¹H H₂O (6.0 ppm) signal and the -80 ppm –F termination ¹⁹F resonance. The lack of signal from the -OH terminations is ascribed to a short ${}^{1}H$ $T_{1\rho}$ for this resonance, so that the transverse magnetization decays before developing significant cross-polarization. The fact that the H₂O resonance correlates only with the -80 ppm ¹⁹F signal suggests that these -F termination environments are associated with interlayer water via hydrogen bonding, whereas those at -190

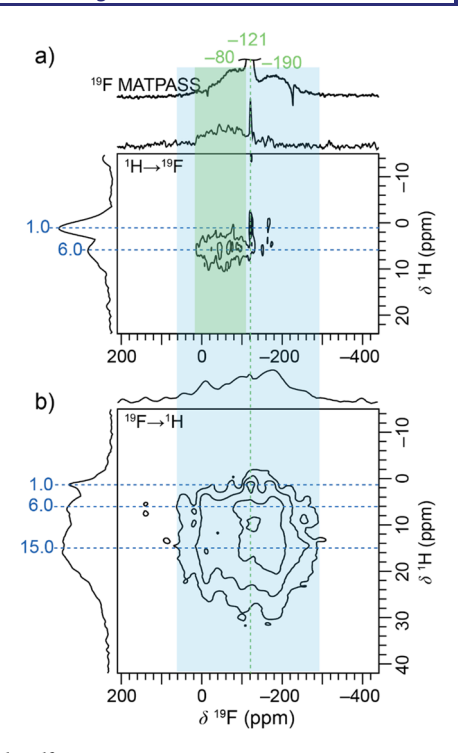


Figure 9. 1 H/ 19 F HETCOR spectra of Nb₄C₃T_x recorded at 11.7 T and 20 kHz MAS with a 2 ms contact time. The recycle delays were 3 and 1 s respectively for panels a and b. The 19 F MATPASS spectrum is shown for comparison. Note that the axes for panel b have been swapped relative to convention to allow comparison of the 19 F axis.

ppm are not. The higher frequency 19 F shift observed for H-bonded –F terminations in Nb₄C₃T_x is also consistent with the assignment of the -20 ppm 19 F signal in Nb₂CT_x to strongly H-bonded –F terminations.

Table 3 shows a comparison of the shifts of the observed surface species for the different MXenes studied by ¹H and ¹⁹F

Table 3. Summary of the Chemical Shifts of ¹H and ¹⁹F Surface Species Observed for Different MXenes

phase	source	δ 1 H/ppm	δ 19 F/ppm
Nb_2CT_x	this work	12.2, 19.5, 26.0	-20, -132
$Nb_4C_3T_x$	this work	15.0	-80, -190
V_2CT_x	Harris et al. ³²	27, 85	-265
$Ti_3C_2T_x$	Hope et al. ³³	12.5/18.6 ^a	$-227/-255^a$
	Anayee et al. ³⁴	15/20 ^a	not attempted
	Kobayashi et al. ³⁵	0.5-2.0, 3.6	"Unable to observe"35

^aDepending on the synthesis procedure.

NMR to date. For the $-\mathrm{OH}$ terminations, $V_2\mathrm{CT}_x$ is the exception with an extremely large shift of 85 ppm; this is due to a metallic Knight shift, as confirmed by the short T_1 relaxation of this signal. Interestingly, the $-\mathrm{F}$ terminations of $V_2\mathrm{CT}_x$ do not appear to be significantly Knight shifted and are observed at a similar frequency to those of $\mathrm{Ti}_3\mathrm{C}_2\mathrm{T}_x$. The $-\mathrm{OH}$ ¹H shifts obtained for $\mathrm{Ti}_3\mathrm{C}_2\mathrm{T}_x$ have been shown by both Hope et al. and Anayee et al. to depend on the synthesis procedure, but in both cases fall in the range 12.5–20 ppm. In contrast, Kobayashi et al. below observed no hardle signals at frequencies above 7 ppm, instead ascribing signals at 0.5–2.0 and 3.6 ppm to $-\mathrm{OH}$ terminations on the basis of DFT calculations and the assignment of a $\mathrm{Ti}_2\mathrm{CT}_x$ has pectrum in a

separate report by Sugahara. 69 These differences may be due to sample preparation, however, we note that the studies of Kobayashi et al. and Sugahara et al. do not provide direct evidence for their terminal –OH assignments (cf. the ${}^{1}H\rightarrow{}^{13}C$ HETCOR employed for V_2CT_x and Ti_3CT_x , 32,33 and the ¹H/⁹³Nb TRAPDOR used here). Furthermore, (i) Sugahara et al. found an estimated composition of Ti₂C- $(OH)_{0.3}O_{0.7}F_{0.6}Cl_{0.4}$ with a similar etching procedure to Kobayashi et al. (LiF and HCl)⁶⁹ and (ii) $Ti_3C_2T_x$ is electronically conducting (so much so that the sample in the Kobayashi et al. study was diluted by a factor of 20 to perform magic angle spinning) but the DFT calculations for -OH shifts include neither -F termination nor Knight shift contributions, which are expected to substantially affect the ¹H shifts.³⁵ It is possible that due to the high conductivity of their samples, Kobayashi et al. and Sugahara et al. are not able to observe the -OH terminations due to rf penetration or bulk magnetic susceptibility broadening effects.

The –OH ¹H shifts for the Nb MXenes are similar to those observed for Ti₃C₂T_x by Hope et al.³³ and Anayee et al.,³⁴ although as the 26 ppm signal for Nb₂CT_x is outside the diamagnetic range for ¹H NMR, there must also be at least a small Knight shift, as for V₂CT_x. The –F terminations, on the other hand, are observed at higher frequencies for the Nb MXenes than for V₂CT_x and Ti₃C₂T_x, which could be due to more covalent Nb–F bonding caused by the more diffuse 4d orbitals. In general, the multiple NMR signals observed for –OH and –F terminations, and the dependence on the synthesis, can be ascribed to distinct local environments due to different arrangements of the surface terminations (–OH, –O, –F, and termination vacancy), as well as interlayer H₂O, as shown, for instance, for the –F terminations in Nb₄C₃T_x.

Extending the Transition-Metal NMR of MAX phases. Based on insights gained from the 93Nb NMR of Nb MAX phases, we were also able to interpret the 47/49Ti NMR of Ti₃AlC₂, another technologically important MAX phase used as a high temperature ceramic, and the precursor to the most studied MXene phase, Ti₃C₂T_x. 5,7,70 Ti NMR is particularly challenging to interpret because its two NMR-active isotopes, ⁴⁷Ti and ⁴⁹Ti, are both quadrupolar (I = 5/2 and 7/2, respectively) and by chance have extremely similar gyromagnetic ratios, differing by only 267 ppm (0.027%). As a result, overlapping quadrupolar lineshapes for both isotopes are typically observed in a single spectrum. 46,71-73 Nevertheless, the ⁴⁷Ti and ⁴⁹Ti signals of both the inner and outer Ti environments in Ti₃AlC₂ could be assigned from the overlapped spectrum (Figure 10) by considering that the C_O values for the outer/inner metal sites are expected to differ by an order of magnitude (cf. 93Nb in Nb₄AlC₃) and by using the fixed relationships between the nuclear properties of 47/49Ti. The isotropic shift and quadrupolar parameters of the two titanium sites for both nuclei are given in Table 4: since the frequency separation and ratio of the quadrupolar coupling constants for the ⁴⁷Ti and ⁴⁹Ti signals are fixed by their respective nuclear properties, there are fewer independent variables than it might seem, and the simultaneous agreement of both signals with the measured spectrum affords a high confidence in the NMR parameters. As also observed for the Nb MAX phases (Table 2), the Ti sites exhibit axial quadrupolar tensors, consistent with the crystallographic symmetry, while the inner site has a modest Co relative to the outer site.

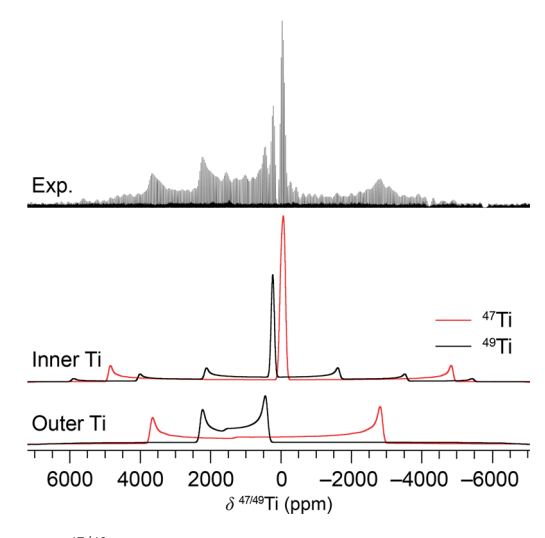


Figure 10. $^{47/49}$ Ti static QCPMG spectrum of Ti₃AlC₂ acquired at 16.4 T by taking the skyline projection of five VOCS subspectra. The simulated quadrupolar 47 Ti and 49 Ti patterns for the inner and outer Ti sites are shown below the experimental spectrum. Simulation parameters are given in Table 4.

Table 4. Fitted 47 Ti and 49 Ti Quadrupolar Parameters for the Two Crystallographic Ti Sites in Ti $_3$ AlC $_2$ Extracted from Figure 10^a

site	nucleus	$\delta_{ ext{iso}} \ (ext{ppm})^{m{b}}$	$C_{\mathbb{Q}}$ (MHz)	η_{Q}
inner	⁴⁷ Ti	-27(10)	2.57 ^c	0.00^{d}
	⁴⁹ Ti	240(10)	2.10^{c}	0.00^{d}
outer	⁴⁷ Ti	1338(20)	18.1(3)	0.00(5)
	⁴⁹ Ti	1605(20)	14.8(2)	0.00(5)

^aThe estimated errors in the last digit are given in parentheses. Note that the simulated spectra were insensitive to the CSA parameters, which were therefore not determined. ^bThe ⁴⁷Ti shifts are referenced to ⁴⁹Ti and as such are 267 ppm less than the corresponding ⁴⁹Ti shift, rather than equal. ^cThis represents an upper bound, based on the line width of the ⁴⁷Ti signal. ^dThe inherent line width is too broad to determine η_Q from the line shape of the central transition, and the turning points of the satellite transitions cannot be identified, however $\eta_Q = 0$ is consistent with the crystallographic symmetry.

CONCLUSIONS

An extensive survey of the NMR properties of the Nb MAX and MXene phases has been presented. The multinuclear approach adopted in this study provides complementary measurements of the local structural and electronic properties of the MAX and MXene phases, identifies the nature and connectivity of MXene surface terminating species, and enables unambiguous detection of a number of impurity phases.

²⁷Al and ⁹³Nb NMR spectra of the MAX phases Nb₂AlC and Nb₄AlC₃ have been recorded under static and MAS conditions with high resolution and wide-line techniques, allowing extraction of the full anisotropic shift and quadrupolar tensors. The insights gained from the Nb MAX phases also then enabled the interpretation of the ^{47/49}Ti spectrum of Ti₃AlC₂. The quadrupolar parameters extracted from the spectra were in close agreement with DFT calculations, affording a detailed view of the local coordination environments. The ²⁷Al, ⁹³Nb, and ¹³C spectra also reveal impurity phases in both Nb₂AlC and Nb₄AlC₃, including aluminum oxide, hydrated aluminum fluoride, aluminum carbide/oxycarbide/nitride, niobium metal, and (nonstoichiometric) NbC_x species. Many of these

impurities are not apparent from diffraction alone and these results should serve as a guide for future synthesis efforts.

Following the etching process, the conversion to form MXenes was confirmed by ¹³C and ⁹³Nb NMR, although the presence of unreacted Nb₂AlC is apparent in the ⁹³Nb, ²⁷Al, and ¹³C spectra of the Nb₂CT_x sample. ⁹³Nb environments become notably more asymmetric in the MXenes compared to the MAX phases, demonstrating the reduction of symmetry at the surface. The quadrupolar coupling is still lower than calculated for a bare surface, however, pointing to the presence of surface terminations; these surface terminations are key in determining the performance of MXenes in various applications. -OH and -F terminations have been identified for both Nb₂CT_x and Nb₄C₃T_x in the ¹H and ¹⁹F NMR spectra, their proximity to the surface demonstrated with ⁹³Nb TRAPDOR experiments, and a comparison made with previous studies on $Ti_3C_2T_x$ and V_2CT_x MXenes. The atomic-scale intermixing of -OH and -F terminations for $Nb_4C_3T_x$ is seen in the ${}^1H/{}^{19}F$ HETCOR spectra, which would be challenging to identify by other techniques, and the different 19F termination environments observed for both MXenes are correlated with the degree of hydrogen bonding to interlayer H2O.

The structural insights derived here should serve as a basis to improve synthetic methods and to guide more in-depth computational modeling, both for the Nb MAX and MXene phases, as well as to facilitate comparisons with the wider family of materials. The nature of the surface terminations and interlayer water in MXenes are key to understanding the functional properties, while further insight into the electronic structure in the MAX phases is of fundamental interest. In this way, structure—property relationships can be developed and both MAX and MXene materials can be optimized for advanced functional applications.

ASSOCIATED CONTENT

Supporting Information

The Supporting Information is available free of charge at https://pubs.acs.org/doi/10.1021/jacs.0c09044.

Diffraction data; additional NMR spectra of Nb₄AlC₃, Nb₂AlC, Nb₄C₃T_x, Nb₂CT_x, Nb₂SnC, and NbC; Nb MAX phase chemical shift tensors tabulated in the standard convention; and tables of ⁹³Nb quadrupolar parameters for bare and terminated Nb MXene surfaces. (PDF)

AUTHOR INFORMATION

Corresponding Author

Clare P. Grey — Department of Chemistry, University of Cambridge, Cambridge CB2 1EW, United Kingdom; orcid.org/0000-0001-5572-192X; Email: cpg27@cam.ac.uk

Authors

Kent J. Griffith — Department of Chemistry, University of Cambridge, Cambridge CB2 1EW, United Kingdom; Department of Chemistry and Department of Materials Science and Engineering, Northwestern University, Evanston, Illinois 60208, United States; orcid.org/0000-0002-8096-906X

Michael A. Hope — Department of Chemistry, University of Cambridge, Cambridge CB2 1EW, United Kingdom; orcid.org/0000-0002-4742-9336

Philip J. Reeves — Department of Chemistry, University of Cambridge, Cambridge CB2 1EW, United Kingdom;
orcid.org/0000-0003-4339-7282

Mark Anayee — A. J. Drexel Nanomaterials Institute, and Department of Materials Science and Engineering, Drexel University, Philadelphia, Pennsylvania 19104, United States; orcid.org/0000-0002-6691-920X

Yury Gogotsi — A. J. Drexel Nanomaterials Institute, and Department of Materials Science and Engineering, Drexel University, Philadelphia, Pennsylvania 19104, United States; orcid.org/0000-0001-9423-4032

Complete contact information is available at: https://pubs.acs.org/10.1021/jacs.0c09044

Author Contributions

K.J.G. and M.A.H. contributed equally.

Notes

The authors declare no competing financial interest.

ACKNOWLEDGMENTS

K.J.G. thanks the Winston Churchill Foundation of the United States and the Herchel Smith Scholarship for financial support. M.A.H. acknowledges funding from the Oppenheimer foundation. K.J.G. and C.P.G. are grateful for support from the EPSRC (EP/M009521/1). M.A. was supported by the National Science Foundation Graduate Research Fellowship under Grant DGE-1646737. Y. G. was supported by the National Science Foundation under Grant No. DMR-1740795. This work made use of the IMSERC X-ray and NMR facility at Northwestern University, which has received support from the National Science Foundation (NSF DMR-0521267), the Soft and Hybrid Nanotechnology Experimental (SHyNE) Resource (NSF ECCS-1542205), the State of Illinois, and the International Institute for Nanotechnology (IIN). Any opinions, findings, and conclusions or recommendations expressed in this material are those of the authors and do not necessarily reflect the views of the National Science Foundation. The authors are grateful to M. Alhabeb and Dr. D. Pinto (Drexel University) for their help with the synthesis of samples for this

REFERENCES

- (1) Sun, Z. M. Progress in Research and Development on MAX Phases: A Family of Layered Ternary Compounds. *Int. Mater. Rev.* **2011**, *56* (3), 143–166.
- (2) Barsoum, M. W. The $M_{N+1}AX_N$ Phases: A New Class of Solids; Thermodynamically Stable Nanolaminates. *Prog. Solid State Chem.* **2000**, 28 (1–4), 201–281.
- (3) Barsoum, M. W.; Radovic, M. Elastic and Mechanical Properties of the MAX Phases. *Annu. Rev. Mater. Res.* **2011**, *41* (1), 195–227.
- (4) Sokol, M.; Natu, V.; Kota, S.; Barsoum, M. W. On the Chemical Diversity of the MAX Phases. *Trends Chem.* **2019**, *1* (2), 210–223.
- (5) Naguib, M.; Kurtoglu, M.; Presser, V.; Lu, J.; Niu, J.; Heon, M.; Hultman, L.; Gogotsi, Y.; Barsoum, M. W. Two-Dimensional Nanocrystals Produced by Exfoliation of Ti₃AlC₂. *Adv. Mater.* **2011**, 23 (37), 4248–4253.
- (6) Radovic, M.; Barsoum, M. W. MAX Phases: Bridging the Gap between Metals and Ceramics. *Am. Ceram. Soc. Bull.* **2013**, 92 (3), 20–27.
- (7) Anasori, B.; Lukatskaya, M. R.; Gogotsi, Y. 2D Metal Carbides and Nitrides (MXenes) for Energy Storage. *Nat. Rev. Mater.* **2017**, *2*, 16098.
- (8) Li, N.; Li, Y.; Zhu, X.; Huang, C.; Kai, J.-J.; Fan, J. Theoretical Investigation of the Structure-Property Correlation of MXenes as

- Anode Materials for Alkali Metal Ion Batteries. J. Phys. Chem. C 2020, 124 (28), 14978–14986.
- (9) Gao, G.; O'Mullane, A. P.; Du, A. 2D MXenes: A New Family of Promising Catalysts for the Hydrogen Evolution Reaction. *ACS Catal.* **2017**, *7* (1), 494–500.
- (10) Su, T.; Peng, R.; Hood, Z. D.; Naguib, M.; Ivanov, I. N.; Keum, J. K.; Qin, Z.; Guo, Z.; Wu, Z. One-Step Synthesis of Nb₂O₅/C/Nb₂C (MXene) Composites and Their Use as Photocatalysts for Hydrogen Evolution. *ChemSusChem* **2018**, *11* (4), 688–699.
- (11) Ma, T. Y.; Cao, J. L.; Jaroniec, M.; Qiao, S. Z. Interacting Carbon Nitride and Titanium Carbide Nanosheets for High-Performance Oxygen Evolution. *Angew. Chem., Int. Ed.* **2016**, 55 (3), 1138–1142.
- (12) Xie, X.; Chen, S.; Ding, W.; Nie, Y.; Wei, Z. An Extraordinarily Stable Catalyst: Pt NPs Supported on Two-Dimensional $\mathrm{Ti}_3\mathrm{C}_2\mathrm{X}_2$ (X = OH, F) Nanosheets for Oxygen Reduction Reaction. *Chem. Commun.* **2013**, 49 (86), 10112–10114.
- (13) Lin, H.; Gao, S.; Dai, C.; Chen, Y.; Shi, J. A Two-Dimensional Biodegradable Niobium Carbide (MXene) for Photothermal Tumor Eradication in NIR-I and NIR-II Biowindows. *J. Am. Chem. Soc.* **2017**, 139 (45), 16235–16247.
- (14) Shahzad, F.; Alhabeb, M.; Hatter, C. B.; Anasori, B.; Man Hong, S.; Koo, C. M.; Gogotsi, Y. Electromagnetic Interference Shielding with 2D Transition Metal Carbides (MXenes). *Science* **2016**, 353 (6304), 1137–1140.
- (15) Song, S.; Liu, J.; Zhou, C.; Jia, Q.; Luo, H.; Deng, L.; Wang, X. Nb₂O₅/Nb₂CT_x Composites with Different Morphologies through Oxidation of Nb₂CT_x MXene for High-Performance Microwave Absorption. *J. Alloys Compd.* **2020**, *843*, 155713.
- (16) Eames, C.; Islam, M. S. Ion Intercalation into Two-Dimensional Transition-Metal Carbides: Global Screening for New High Capacity Battery Materials. *J. Am. Chem. Soc.* **2014**, *136* (46), 16270–16276.
- (17) Kim, H.; Alshareef, H. N. MXetronics: MXene-Enabled Electronic and Photonic Devices. *ACS Mater. Lett.* **2020**, 2 (1), 55–70.
- (18) Kamysbayev, V.; Filatov, A. S.; Hu, H.; Rui, X.; Lagunas, F.; Wang, D.; Klie, R. F.; Talapin, D. V. Covalent Surface Modifications and Superconductivity of Two-Dimensional Metal Carbide MXenes. *Science* **2020**, *369* (6506), 979–983.
- (19) Jeitschko, W.; Nowotny, H.; Benesovsky, F. Kohlenstoffhaltige ternäre Verbindungen (H-Phase). *Monatsh. Chem.* **1963**, *94*, *672*–676.
- (20) Jeitschko, W.; Nowotny, H.; Benesovsky, F. Die H-Phasen Ti₂TlC, Ti₂PbC, Nb₂InC, Nb₂SnC und Ta₂GaC. *Monatsh. Chem.* **1964**, 95, 431–435.
- (21) Hu, C.; Li, F.; Zhang, J.; Wang, J.; Wang, J.; Zhou, Y. Nb₄AlC₃: A New Compound Belonging to the MAX Phases. *Scr. Mater.* **2007**, 57 (10), 893–896.
- (22) Naguib, M.; Halim, J.; Lu, J.; Cook, K. M.; Hultman, L.; Gogotsi, Y.; Barsoum, M. W. New Two-Dimensional Niobium and Vanadium Carbides as Promising Materials for Li-Ion Batteries. *J. Am. Chem. Soc.* **2013**, *135* (43), 15966–15969.
- (23) Ghidiu, M.; Naguib, M.; Shi, C.; Mashtalir, O.; Pan, L. M.; Zhang, B.; Yang, J.; Gogotsi, Y.; Billinge, S. J. L.; Barsoum, M. W. Synthesis and Characterization of Two-Dimensional Nb_4C_3 (MXene). *Chem. Commun.* **2014**, *50* (67), 9517–9520.
- (24) Bai, Y.; He, X.; Wang, R. Lattice Dynamics of Al-Containing MAX-Phase Carbides: A First-Principle Study. *J. Raman Spectrosc.* **2015**, 46 (9), 784–794.
- (25) Ren, X.; Huo, M.; Wang, M.; Lin, H.; Zhang, X.; Yin, J.; Chen, Y.; Chen, H. Highly Catalytic Niobium Carbide (MXene) Promotes Hematopoietic Recovery after Radiation by Free Radical Scavenging. ACS Nano 2019, 13 (6), 6438–6454.
- (26) Wang, Y.; Wang, Y.; Chen, K.; Qi, K.; Xue, T.; Zhang, H.; He, J.; Xiao, S. Niobium Carbide MXenes with Broad-Band Nonlinear Optical Response and Ultrafast Carrier Dynamics. *ACS Nano* **2020**, *14* (8), 10492–10502.

- (27) Zhao, S.; Meng, X.; Zhu, K.; Du, F.; Chen, G.; Wei, Y.; Gogotsi, Y.; Gao, Y. Li-Ion Uptake and Increase in Interlayer Spacing of Nb₄C₃ MXene. *Energy Storage Mater.* **2017**, *8*, 42–48.
- (28) Lipatov, A.; Alhabeb, M.; Lu, H.; Zhao, S.; Loes, M. J.; Vorobeva, N. S.; Dall'Agnese, Y.; Gao, Y.; Gruverman, A.; Gogotsi, Y.; Sinitskii, A. Electrical and Elastic Properties of Individual Single-Layer Nb₄C₃T_x MXene Flakes. *Adv. Electron. Mater.* **2020**, *6* (4), 1901382.
- (29) Bortolozo, A. D.; Sant'Anna, O. H.; da Luz, M. S.; dos Santos, C. A. M.; Pereira, A. S.; Trentin, K. S.; Machado, A. J. S. Superconductivity in the Nb₂SnC Compound. *Solid State Commun.* **2006**, 139 (2), 57–59.
- (30) Scabarozi, T. H.; Roche, J.; Rosenfeld, A.; Lim, S. H.; Salamanca-Riba, L.; Yong, G.; Takeuchi, I.; Barsoum, M. W.; Hettinger, J. D.; Lofland, S. E. Synthesis and Characterization of Nb₂AlC Thin Films. *Thin Solid Films* **2009**, *517* (9), 2920–2923.
- (31) Lue, C. S.; Lin, J. Y.; Xie, B. X. NMR Study of the Ternary Carbides M₂AlC (M = Ti, V, Cr). *Phys. Rev. B: Condens. Matter Mater. Phys.* **2006**, 73 (3), 035125.
- (32) Harris, K. J.; Bugnet, M.; Naguib, M.; Barsoum, M. W.; Goward, G. R. Direct Measurement of Surface Termination Groups and Their Connectivity in the 2D MXene V₂CT_x Using NMR Spectroscopy. *J. Phys. Chem. C* **2015**, *119*, 13713–13720.
- (33) Hope, M. A.; Forse, A. C.; Griffith, K. J.; Lukatskaya, M. R.; Ghidiu, M.; Gogotsi, Y.; Grey, C. P. NMR Reveals the Surface Functionalisation of Ti₃C₂ MXene. *Phys. Chem. Chem. Phys.* **2016**, *18* (7), 5099–5102.
- (34) Anayee, M.; Kurra, N.; Alhabeb, M.; Seredych, M.; Hedhili, M. N.; Emwas, A.-H.; Alshareef, H. N.; Anasori, B.; Gogotsi, Y. Role of Acid Mixtures Etching on the Surface Chemistry and Sodium Ion Storage in Ti₃C₂T_x MXene. *Chem. Commun.* **2020**, *56* (45), 6090–6093.
- (35) Kobayashi, T.; Sun, Y.; Prenger, K. E.; Jiang, D.-E.; Naguib, M.; Pruski, M. Nature of Terminating Hydroxyl Groups and Intercalating Water in Ti₃C₂T_x MXenes: A Study by ¹H Solid-State NMR and DFT Calculations. *J. Phys. Chem. C* **2020**, *124* (25), 13649–13655.
- (36) Hung, I.; Zhou, L.; Pourpoint, F.; Grey, C. P.; Gan, Z. Isotropic High Field NMR Spectra of Li-Ion Battery Materials with Anisotropy > 1 MHz. *J. Am. Chem. Soc.* **2012**, *134* (4), 1898–1901.
- (37) Pecher, O.; Halat, D. M.; Lee, J.; Liu, Z.; Griffith, K. J.; Braun, M.; Grey, C. P. Enhanced Efficiency of Solid-State NMR Investigations of Energy Materials Using an External Automatic Tuning/Matching (eATM) Robot. J. Magn. Reson. 2017, 275, 127–136.
- (38) Lipton, A. S.; Wright, T. A.; Bowman, M. K.; Reger, D. L.; Ellis, P. D. Solid-State ⁶⁷Zn NMR Spectroscopy in Bioinorganic Chemistry. Spectra of Four- and Six-Coordinate Zinc Pyrazolylborate Complexes Obtained by Management of Proton Relaxation Rates with a Paramagnetic Dopant. *J. Am. Chem. Soc.* **2002**, *124* (20), 5850–5860.
- (39) Prasad, S.; Zhao, P.; Huang, J.; Fitzgerald, J. J.; Shore, J. S. Niobium-93 MQMAS NMR Spectroscopic Study of Alkali and Lead Niobates. *Solid State Nucl. Magn. Reson.* **2001**, *19* (1), 45–62.
- (40) Stone, N. J. Table of Nuclear Electric Quadrupole Moments. At. Data Nucl. Data Tables 2016, 111, 1-28.
- (41) Clark, S. J.; Segall, M. D.; Pickard, C. J.; Hasnip, P. J.; Probert, M. I. J.; Refson, K.; Payne, M. C. First Principles Methods using CASTEP. Z. Kristallogr. Cryst. Mater. 2005, 220 (5–6), 567–570.
- (42) Perdew, J. P.; Burke, K.; Ernzerhof, M. Generalized Gradient Approximation Made Simple. *Phys. Rev. Lett.* **1996**, 77 (18), 3865–3868.
- (43) Vanderbilt, D. Soft Self-Consistent Pseudopotentials in a Generalized Eigenvalue Formalism. *Phys. Rev. B: Condens. Matter Mater. Phys.* **1990**, 41 (11), 7892–7895.
- (44) Monkhorst, H. J.; Pack, J. D. Special points for Brillouin-zone Integrations. *Phys. Rev. B* **1976**, *13* (12), 5188–5192.
- (45) Jakobsen, H. J; Skibsted, J.; Bildsøe, H.; Nielsen, N. C. Magic-Angle Spinning NMR Spectra of Satellite Transitions for Quadrupolar Nuclei in Solids. *J. Magn. Reson.* **1989**, *85*, 173–180.

- (46) Mackenzie, K. J. D.; Smith, M. E. Multinuclear Solid-State NMR of Inorganic Materials; Pergamon Materials Series; Pergamon: London, 2002; Vol. 6.
- (47) Myhra, S.; Crossley, J. A. A.; Barsoum, M. W. Crystal-Chemistry of the Ti₃AlC₂ and Ti₄AlN₃ Layered Carbide/Nitride Phases—Characterization by XPS. *J. Phys. Chem. Solids* **2001**, *62* (4), 811–817.
- (48) Bräuniger, T.; Jansen, M. Solid-State NMR Spectroscopy of Quadrupolar Nuclei in Inorganic Chemistry. Z. Anorg. Allg. Chem. **2013**, 639 (6), 857–879.
- (49) Bräuniger, T.; Chandran, C. V.; Wedig, U.; Jansen, M. NMR Chemical Shift and Quadrupolar Interaction Parameters of Carbon-Coordinated ²⁷Al in Aluminium Carbide, Al₄C₃. *Z. Anorg. Allg. Chem.* **2011**, *637* (5), 530–535.
- (50) Marti, R. M.; Sarou-Kanian, V.; Moran, C. M.; Walton, K. S.; Hayes, S. E. NMR Crystallography of Aluminum Carbide: Impurities in the Reagent and Improved ²⁷Al NMR Tensors. *J. Phys. Chem. C* **2020**, 124 (13), 7238–7243.
- (51) Butler, N. D.; Dupree, R.; Lewis, M. H. The Use of Magic-Angle-Spinning NMR in Structural Studies of Si-Al-O-N Phases. *J. Mater. Sci. Lett.* **1984**, 3 (5), 469–470.
- (52) Dupree, R.; Lewis, M. H.; Smith, M. E. Structural Characterization of Ceramic Phases with High-Resolution ²⁷Al NMR. *J. Appl. Crystallogr.* **1988**, *21*, 109–116.
- (53) Bräuniger, T.; Kempgens, P.; Harris, R. K.; Howes, A. P.; Liddell, K.; Thompson, D. P. A Combined 14 N/ 27 Al Nuclear Magnetic Resonance and Powder X-Ray Diffraction Study of Impurity Phases in β-Sialon Ceramics. *Solid State Nucl. Magn. Reson.* **2003**, 23 (1–2), 62–76.
- (54) Cozzan, C.; Griffith, K. J.; Laurita, G.; Hu, J. G.; Grey, C. P.; Seshadri, R. Structural Evolution and Atom Clustering in β -SialON: β -Si_{6-x}Al₂O_xN_{8-x}. *Inorg. Chem.* **2017**, *56* (4), 2153–2158.
- (55) Kim, H. S.; Bugli, G.; Djéga-Mariadassou, G. Preparation and Characterization of Niobium Carbide and Carbonitride. *J. Solid State Chem.* 1999, 142 (1), 100–107.
- (56) Rempel, A. A.; Gusev, A. I.; Belyaev, M. Y. ⁹³Nb NMR Study of an Ordered and a Disordered Non-Stoichiometric Niobium Carbide. *J. Phys. C: Solid State Phys.* **1987**, 20 (34), 5655–5666.
- (57) Froidevaux, C.; Rossier, D. N.M.R. Investigation of the Atomic and Electronic Structure of Vanadium and Niobium Carbides. *J. Phys. Chem. Solids* **1967**, 28 (7), 1197–1209.
- (58) Sarycheva, A.; Gogotsi, Y. Raman Spectroscopy Analysis of the Structure and Surface Chemistry of $Ti_3C_2T_x$ MXene. *Chem. Mater.* **2020**, 32 (8), 3480–3488.
- (59) Mashtalir, O.; Lukatskaya, M. R.; Zhao, M.-Q.; Barsoum, M. W.; Gogotsi, Y. Amine-Assisted Delamination of Nb₂C MXene for Li-Ion Energy Storage Devices. *Adv. Mater.* **2015**, *27* (23), 3501–3506.
- (60) Cockreham, C. B.; Zhang, X.; Li, H.; Hammond-Pereira, E.; Sun, J.; Saunders, S. R.; Wang, Y.; Xu, H.; Wu, D. Inhibition of AlF₃: 3H₂O Impurity Formation in Ti₃C₂T_x MXene Synthesis under a Unique CoF_x/HCl Etching Environment. *ACS Appl. Energy Mater.* **2019**, 2 (11), 8145–8152.
- (61) Deeva, E. B.; Kurlov, A.; Abdala, P. M.; Lebedev, D.; Kim, S. M.; Gordon, C. P.; Tsoukalou, A.; Fedorov, A.; Müller, C. R. In Situ XANES/XRD Study of the Structural Stability of Two-Dimensional Molybdenum Carbide Mo₂CT_x: Implications for the Catalytic Activity in the Water–Gas Shift Reaction. *Chem. Mater.* **2019**, *31* (12), 4505–4513.
- (62) Seredych, M.; Shuck, C. E.; Pinto, D.; Alhabeb, M.; Precetti, E.; Deysher, G.; Anasori, B.; Kurra, N.; Gogotsi, Y. High-Temperature Behavior and Surface Chemistry of Carbide MXenes Studied by Thermal Analysis. *Chem. Mater.* **2019**, *31* (9), 3324–3332.
- (63) Grey, C. P.; Vega, A. J. Determination of the Quadrupole Coupling Constant of the Invisible Aluminum Spins in Zeolite HY with ¹H/²⁷Al TRAPDOR NMR. *J. Am. Chem. Soc.* **1995**, *117* (31), 8232–8242.
- (64) Persson, I.; Halim, J.; Hansen, T. W.; Wagner, J. B.; Darakchieva, V.; Palisaitis, J.; Rosen, J.; Persson, P. O. Å. How

- Much Oxygen Can a MXene Surface Take Before It Breaks? Adv. Funct. Mater. 2020, 1909005.
- (65) König, R.; Scholz, G.; Pawlik, A.; Jäger, C.; van Rossum, B.; Kemnitz, E. Identification of $AlF_x(OR)_y$ Species in Strongly Disordered Aluminum Isopropoxide Fluoride Solids: A Field-Dependent MAS NMR Study. *J. Phys. Chem. C* **2009**, *113* (35), 15576–15585.
- (66) Mouras, S.; Hamwi, A.; Djurado, D.; Cousseins, J. C.; Fawal, Z.; Mohamad, A. H.; Dupuis, J. ¹⁹F NMR Study of Niobium Pentafluoride-Graphite Intercalation Compounds Prepared under Fluorine Atmosphere. *J. Solid State Chem.* **1989**, 83 (1), 115–120.
- (67) Bloch, F.; Siegert, A. Magnetic Resonance for Nonrotating Fields. *Phys. Rev.* **1940**, *57* (6), 522–527.
- (68) Emsley, L.; Bodenhausen, G. Phase Shifts Induced by Transient Bloch–Siegert Effects in NMR. *Chem. Phys. Lett.* **1990**, *168* (3–4), 297–303.
- (69) Sugahara, A.; Ando, Y.; Kajiyama, S.; Yazawa, K.; Gotoh, K.; Otani, M.; Okubo, M.; Yamada, A. Negative Dielectric Constant of Water Confined in Nanosheets. *Nat. Commun.* **2019**, *10*, 850.
- (70) Tzenov, N. V.; Barsoum, M. W. Synthesis and Characterization of Ti₃AlC₂. *J. Am. Ceram. Soc.* **2000**, 83 (4), 825–832.
- (71) Lucier, B. E. G.; Huang, Y. Reviewing ^{47/49}Ti Solid-State NMR Spectroscopy: From Alloys and Simple Compounds to Catalysts and Porous Materials. In *Annu. Rep. NMR Spectrosc.*; Webb, G. A., Ed.; Academic Press: New York, 2016; Vol. 88, Chapter 1, pp 1–78.
- (72) Xu, J.; Lucier, B. E. G.; Lin, Z.; Sutrisno, A.; Terskikh, V. V.; Huang, Y. New Insights into the Short-Range Structures of Microporous Titanosilicates As Revealed by ^{47/49}Ti, ²³Na, ³⁹K, and ²⁹Si Solid-State NMR Spectroscopy. *J. Phys. Chem. C* **2014**, *118* (47), 27353–27365.
- (73) He, P.; Lucier, B. E. G.; Terskikh, V. V.; Shi, Q.; Dong, J.; Chu, Y.; Zheng, A.; Sutrisno, A.; Huang, Y. Spies within Metal-Organic Frameworks: Investigating Metal Centers Using Solid-State NMR. *J. Phys. Chem. C* **2014**, *118* (41), 23728–23744.